

Crystalline $\text{Co}_2\text{V}_3\text{O}_8$ @Amorphous Co–B Core–Shell Nano-Microsphere: Tunable Shell Layer Thickness, Faradaic Pseudocapacitive Mechanism, and Electrochemical Capacitor Applications

Jing-Feng Hou,^[a] Jian-Fei Gao,^[a] and Ling-Bin Kong^{*[a, b]}

The interface engineering of highly efficient electrode materials is of dominant importance for enhancing the electrochemical performance of advanced energy storage devices. Here, we demonstrate the construction of a novel crystalline@amorphous core–shell nanostructured with $\text{Co}_3\text{V}_2\text{O}_8$ spherical particles as the cores and Co–B nanoflakes as the shells. The Co–B shell layer thickness could be tuned by changing the mass ratio of $\text{Co}_3\text{V}_2\text{O}_8$ and B source. This unique structure shows intriguing synergistic properties with increased electroactive sites and also provides effective space and a short diffusion distance for

faradaic reactions. The tunable amorphous layer facilitates the electrolyte diffusion while showing elastic behavior to alleviate the volume strain of $\text{Co}_3\text{V}_2\text{O}_8$, and also provides a path for electron transport. The resulting $\text{Co}_3\text{V}_2\text{O}_8$ @Co–B under optimum conditions exhibits a high specific capacitance, remarkable rate performance, and outstanding cycling stability. Such an effective redox approach may shed substantial light on inspiring crystalline/amorphous contacts and their derivatives for energy storage and conversion devices.

1. Introduction

The large-scale application of advanced energy storage equipment promotes the rapid development of human society and the new energy industry.^[1–3] Among the potential candidates, transition metal oxides have emerged to be one of the most promising electrode materials for supercapacitors, Li-ion batteries, and so on.^[4–6] Their large theoretical specific capacitances originated from multiple valence changes on transition metals.^[7] In particular, binary metal oxides, which have a better electrochemical character than the corresponding single-component oxides, probably due to their more abundant oxidation states and higher electrochemical activity, are considered as promising, effective, and scalable alternatives.^[8–10] Nevertheless, the Faraday reaction involving ion transport and charge transfer is demanding with respect to kinetics and stability, thus greatly hindering the large-scale applications of binary transition metal oxides.^[11–12] Consequently, it is crucial that the conductivity needs to be enhanced to support rapid electron transfer to match ion transport for efficient kinetics.^[13]

To solve this problem, the best strategy is to synthesis hybrid materials by adding conductive additives.^[14]

Various works have shown that carbon hybridization can significantly improve the conductivity of oxides and have shown increased capacitive properties to some extent.^[15–16] Teng et al.^[17] synthesized coaxial carbon@ NiMoO_4 nanofibers to form a hierarchical structure, which enhances the conductivity as well as the porosity of the electrode, resulting in an outstanding specific capacitance of 1840 F g^{-1} at 1 A g^{-1} . Unfortunately, the potential window of carbon is generally between -1 – 0 V , which does not substantially overlap with the potential window of the anode material, thus providing little specific capacitance at the positive potential. The recent development of non-carbon heterogeneous interfaces endows hybrid materials with unique character and potential applications.^[18] Mai et al.^[19] fabricated hierarchical $\text{MnMoO}_4/\text{CoMoO}_4$ heterostructured nanowires, which display a specific capacitance of 187.1 F g^{-1} at 1 A g^{-1} . However, the lattice and electron mismatches sometimes occurred at the interfaces due to contact of different crystals, which creates a new barrier and limits the transfer of ions and electrons.^[20] The amorphous phase is promising to be one of the solutions and its inherent disordered arrangement and structural imperfections are indicated to be highly constructive to promote the diffusion of ions.^[21] The loosely packed structure and isotropic properties of the amorphous phase can effectively accommodate the volume variation and mitigate the volume effects during the redox process, benefiting to high the specific capacitance and cyclic stability.^[22] Deng et al.^[23] constructed a compact $\text{ZnCo}_2\text{O}_4/\text{Co–B}$ hybrid structure, in which the amorphous Co–B nanoflakes not only act as effective electron conduction bridge to facilitate rapid electron transportation, but the mesopores in Co–B

[a] J.-F. Hou, J.-F. Gao, Prof. L.-B. Kong
State Key Laboratory of Advanced Processing and Recycling of Non-ferrous Metals
Lanzhou University of Technology
Lanzhou 730050, P. R. China
Fax: (+86) (0)931 2976578
E-mail: konglb@lut.edu.cn

[b] Prof. L.-B. Kong
School of Materials Science and Engineering
Lanzhou University of Technology
Lanzhou 730050, P. R. China

 Supporting information for this article is available on the WWW under
<https://doi.org/10.1002/batt.202100022>

nanoflakes support to overcome the ion diffusion barriers. The introduction of crystalline/ amorphous contacts greatly affects the transport of carriers and the Faraday reaction process.

So far, there are many reports on crystalline-amorphous interface engineering for energy storage and electrocatalysis. Wang and co-workers^[24] tuned the crystalline and electronic structures of Co–Ni MOFs by introducing NaBH₄ to activate the conductivity and electrochemical performance. The obtained cobalt/nickel boride/ sulfide enables fast faraday reaction and shows an excellent specific capacitance and superior cycling stability. Slabon et al.^[25] synthesized MB (M=Co, Fe) modified WO₃ photoanodes with high catalytic enhancement, which emphasized the role of the semiconductor-electrocatalyst interface for photoelectrodes. In addition to the material combination, it has become the focus of research to achieve precise control of the microscopic morphology of electrode materials, maximize their structural advantages.^[26] The core-shell structure of electrode materials has been proved as a promising strategy to improve electrochemical properties by effectually alleviating the stress-induced structural changes during long-term electrochemical reactions.^[27] In particular, the spherical structures have aroused great research interest because of their structural advantages with complex variant voids, larger specific surface area, more active sites, and tunable core-shell combinations compared with the nanowires structures.

Based on the above considerations, we demonstrate a facile and scalable avenue to rationally construct well-constructed hybrid architectures, which is to coat ultrathin amorphous Co–B nanoflakes on crystalline Co₃V₂O₈ spherical particles (expressed as Co₃V₂O₈@Co–B), via a facile two-step water bath coprecipitation and redox process. And the Co–B shell thickness could be tuned. This unique structure leads to the increased electrochemical active sites, modulated surface electronic structure, and more ion diffusion channels. More importantly, the amorphous Co–B layer is introduced to protect Co₃V₂O₈ from direct exposure to the electrolyte and can accommodate the volume expansion during charging and release, as well as the two substances interact to form a relatively stable low-valence mixed state. With these properties, the as-obtained Co₃V₂O₈@Co–B exhibits enhanced electrochemical performances, including high specific capacitance, great rate capability, and superior cyclic stability. The asymmetric supercapacitor with high energy density is also assembled and shows excellent electrochemical character. The crystalline-amorphous interface engineering opens up a new window for application in energy storage and conversion devices.

2. Results and Discussion

2.1. Morphology and Structure Characterization

The synthesis procedure of the Co₃V₂O₈@Co–B composite is schematically shown in Figure 1a(see the Experimental section for the detailed formation process). First, the Na₃O₄V solution is added dropwise to the CoCl₂ solution, and the Co₃V₂O₈

nanoparticles are obtained via water bath at 70 °C for 6 h. Subsequently, the dried precursors are ultrasonically dispersed in the CoCl₂ solution and introduce the N₂ to remove dissolved oxygen. Then, the mixed solution of NaBH₄ and NaOH is added dropwise to the above solution. The thickness of the Co–B shell layer can be tuned by changing the mass ratio of Co₃V₂O₈ and B source. The crystal phase purity of the synthesized samples is recorded on X-ray diffraction (XRD). XRD pattern of Co₃V₂O₈@Co–B-2 is exhibited in Figure 1b, in which the diffraction peaks are ascribed to Co₃V₂O₈ (JCPDS 16-0675) and Co–B.^[28–29] The XRD pattern of Co₃V₂O₈ (Figure 1c) shows characteristic peaks located at 2θ = 15.06°, 35.74°, 43.56°, 57.60°, and 63.25° which attributed to the (110), (311), (200), (400), (511), and (440) planes, respectively.^[30] Figure 1d shows the amorphous diffraction peak of Co–B, which is related to the extreme feature of the synthetic reduction reaction.^[31–33] Moreover, the element analysis of the sample is characterized by Energy Dispersive Spectroscopy (EDS). In Figure 1e, the elements of Co, V, O, and B can be detected in the Co₃V₂O₈@Co–B-2 sample. As shown in Figure 1f and 1g, EDS analysis confirms the presence of the corresponding atoms, which shows the successful synthesis of Co₃V₂O₈ and Co–B.

X-ray Photoelectron Spectroscopy (XPS) is measured to analyze the elemental composition and surface electronic states. The wide-scan XPS survey scans of Co₃V₂O₈@Co–B-2, Co₃V₂O₈, and Co–B samples are shown in Figure 2a-I. The distinctive peaks assigned to the B 1s, O 1s, Co 2p, and V 2p are evident from the full-scale XPS spectra of Co₃V₂O₈@Co–B-2, indicating the existence of these elements in the Co₃V₂O₈@Co–B-2 nanocomposites. The strong diffraction peak emerging at 283.5 eV corresponds to C 1s.^[34–35] Figure 2a-II shows the magnified Co 2p peak of all samples. The Co 2p peaks in the whole spectrum can be decomposed into two characteristic peaks (Co₃V₂O₈@Co–B-2: 781.3 and 797.3 eV; Co₃V₂O₈: 781.5 and 797.4 eV; Co–B: 781.5 and 797.4 eV) corresponding to 2p3/2 and 2p1/2, respectively, and two satellite peaks (Co₃V₂O₈@Co–B-2: 786.5 and 803.3 eV; Co₃V₂O₈: 786.9 and 803.1 eV; Co–B: 786.4 and 803.4 eV).^[36] This result is consistent with the electronic combination of Co²⁺ described in the previous report.^[37–38] The V 2p scan shown in Figure 2a-III reveals peaks corresponding to the spin-orbit energy states of V 2p1/2 and V 2p3/2 at binding energies of 524.5/523.1 eV (Co₃V₂O₈: 524.7/523.8 eV) and 518.3/516.9 eV (Co₃V₂O₈: 517.7/516.8 eV), respectively.^[39] Two peaks of 524.5 and 518.3 eV (Co₃V₂O₈: 524.7 and 517.7 eV) can be typically attributed to the presence of V⁵⁺ oxidation state. The other two peaks indicate the presence of V⁴⁺ oxidation state.^[40] The only peak of the O 1s XPS spectrum (Figure 2a-IV) is located at 531.3 eV (Co₃V₂O₈: 530.8 eV), which are attributed to the metal-oxygen bond.^[41] In Figure 2a-V, the peaks at 191.9 and 188.1 eV for Co–B correspond to the presence of B–O and the interaction between B and Co, respectively.^[42–43] It is the likely oxidation of Co–B sample surface under atmospheric conditions.^[44] For Co₃V₂O₈@Co–B-2, the B 1s spectrum consists of a peak at 192.6 eV. The obvious fading of the Co–B bond peak is possibly due to the inhibitory effect of the Co₃V₂O₈ signal on Co–B.^[45]

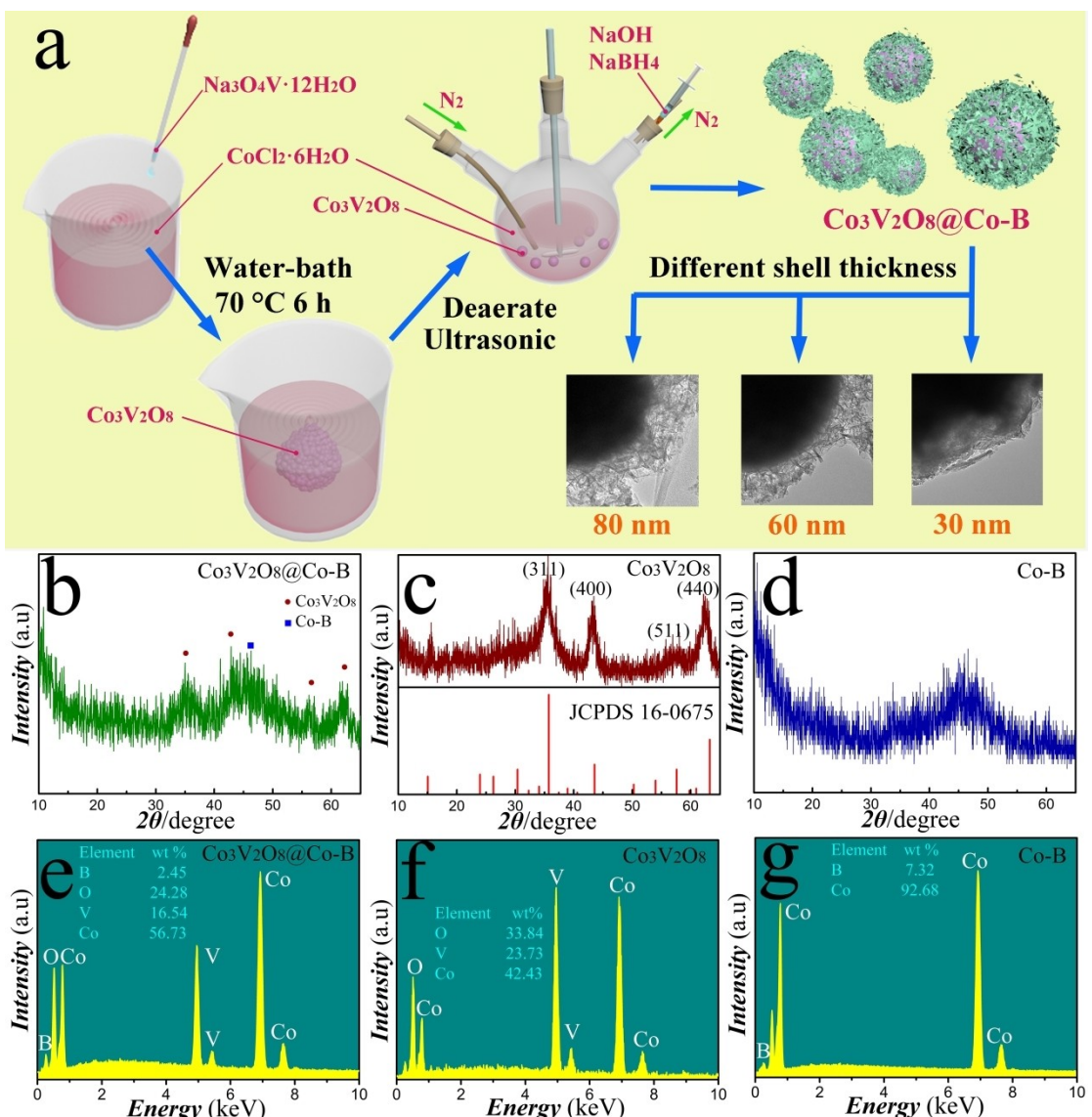


Figure 1. a) The schematic of the synthesis procedure of Co₃V₂O₈@Co-B. XRD and EDS patterns of the samples: b, e) Co₃V₂O₈@Co-B-2, c, f) Co₃V₂O₈, and d, g) Co-B.

The morphologies and microstructure of products are investigated by scanning electron microscopy (SEM) and transmission electron microscope (TEM). The ideal microstructure and morphology of the samples are displayed in Figure 2b-d, which correspond to the SEM images in Figure 2e-g and Figure S1. The TEM images and SAED patterns of the samples are shown in Figure S2. As displayed in Figure 2e, the Co₃V₂O₈ just consists of a great number of nanoparticles, which are loosely packed to form a porous structure. The as-prepared Co-B (Figure 2f) exhibits crumpled and connected nanoflakes with abundant interval space to each other, which facilitate the ions transporting and accommodate the volume expansion. Figure 2g exhibits the SEM images of Co₃V₂O₈@Co-B-2 core/shell heterostructures. Obviously, the Co₃V₂O₈@Co-B-2 is comprised of nanospheres with a diameter of 200 nm. It can be clearly seen that Co₃V₂O₈ is dispersedly arranged and totally covered by Co-B nanoflakes, thereby forming nanospheres

with rough surfaces. Noticeably, such unique structural features would provide abundant space and electroactive sites of Co₃V₂O₈@Co-B electrode, rendering facility electrolyte penetration.

The forming mechanism of the Co₃V₂O₈@Co-B core-shell nanostructures and the precise distribution of the two phases are shown in Figure 3. The growth mechanism of this unique nanostructure is clarified as follows: The Co₃V₂O₈ nanospheres and CoCl₂ are ultrasonic dispersion in the solution. In this process, the Co²⁺ ions will adhere to the surface of the Co₃V₂O₈ nanospheres, where the Co₃V₂O₈ nanospheres serve as the core of the core-shell nanostructure. Subsequent boronization converts Co²⁺ on the surface of the nanospheres into Co-B nanoflakes, which act as core-shell nanostructure shells. The SEM image in Figure 3b shows uniformly distributed Co₃V₂O₈@Co-B-2 nanospheres with rough surfaces. It can be seen from TEM images that the “rough surfaces” are the Co-B

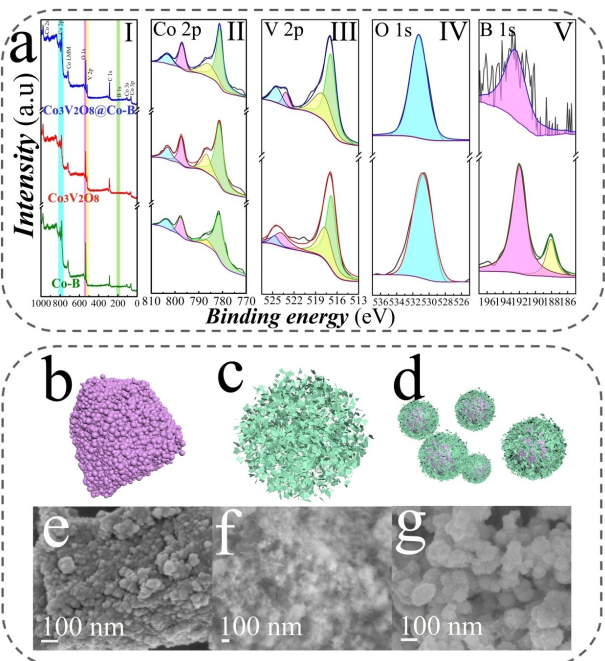


Figure 2. a) XPS spectra of $\text{Co}_3\text{V}_2\text{O}_8@\text{Co-B-2}$, $\text{Co}_3\text{V}_2\text{O}_8$, and Co-B samples. Schematic drawing and SEM images of the samples: b, e) $\text{Co}_3\text{V}_2\text{O}_8$, c, f) Co-B , and d, g) $\text{Co}_3\text{V}_2\text{O}_8@\text{Co-B-2}$.

nanoflakes shell layers, which are interconnected with each other to form an independent network.^[46] The electrolyte can easily diffuse to the surface of the electrode material, most electroactive sites can be effectively used in the charge storage process. Furthermore, the corresponding elemental mapping results of $\text{Co}_3\text{V}_2\text{O}_8@\text{Co-B-2}$ (Figure 3e) indicate the existence of Co, B, V, and O elements and form a core-shell architecture.

The concentration of the reactant solution has been discovered to be critical in determining the morphology of the $\text{Co}_3\text{V}_2\text{O}_8@\text{Co-B}$ core-shell nanostructures. The TEM measurement further confirms the phase distribution of the hybrid. As shown in Figure 3f, 3g, and 3h, when the concentration of the reactant $\text{Co}_3\text{V}_2\text{O}_8$ is halved, that is the mass ratio of $\text{Co}_3\text{V}_2\text{O}_8$ to Co-B is 1:1, the generated Co-B nanoflakes enwrap the $\text{Co}_3\text{V}_2\text{O}_8$ and are prone to grow into large nanosheets assemblies outside the $\text{Co}_3\text{V}_2\text{O}_8@\text{Co-B}$ core-shell nanostructures. On the contrary, when the concentration of reactants increases, that is the mass ratio of $\text{Co}_3\text{V}_2\text{O}_8$ to Co-B is 3:1, only a small amount of Co-B nanoflakes can coat $\text{Co}_3\text{V}_2\text{O}_8$. When the reactant concentration is moderate, the produced Co-B nanoflakes completely cover $\text{Co}_3\text{V}_2\text{O}_8$ and there are almost no large-scale nanosheets other than the core-shell structure. Such morphological variations can be attributed to the different growth kinetics under different reactant concentrations. The TEM observation in Figure 3g, 3k, and 3o exhibit crystalline- $\text{Co}_3\text{V}_2\text{O}_8$ @ amorphous- Co-B core-shell heterogeneous nanostructures with different core@ shell size ratios. As the content of $\text{Co}_3\text{V}_2\text{O}_8$ increases, the thickness of the shell gradually becomes thinner. In Figure 3h, 3l, and 3p, there can be observed the clear crystalline $\text{Co}_3\text{V}_2\text{O}_8$ / amorphous Co-B heterointerfaces. The measured interplanar spacing of

0.251 nm corresponds to the (311) plane of $\text{Co}_3\text{V}_2\text{O}_8$.^[40] The corresponding particle size distribution diagram and frequency curve are drawn according to Figure 3f, 3g, and 3n, respectively. It can be seen in Figure 3j that the particle size of $\text{Co}_3\text{V}_2\text{O}_8@\text{CoB-2}$ is concentrated around 150 nm. Subsequently, the specific surface area and pore size distribution of the sample are also analyzed, and the results are shown in Figure S3. In addition, there is no doubt that morphology changes are of paramount importance for the electrochemical properties, which will be confirmed in subsequent electrochemical tests.

2.2. BET Specific Surface Area Analysis

To assess the specific surface area (SSA) and porosity properties of the prepared samples, N_2 adsorption-desorption tests are performed, of which the results are shown in Figure 4. All products have a large number of mesoporous as they demonstrate type IV isotherms with hysteresis loops (Figure 4a).^[47] In Figure 4b, the pore volume accumulation curve is near-horizontal in the range of 0.4–2.0 nm and gradually increases after about 3 nm. As exhibited in Figure 4c and 4d, the pore size distribution curves show distinct peaks at 1 nm and 4 nm. It can be observed in Figure 4e that $\text{Co}_3\text{V}_2\text{O}_8$ has the highest SSA, while Co-B has the smallest SSA. The SSA of $\text{Co}_3\text{V}_2\text{O}_8@\text{Co-B}$ is between the two, and the SSA of $\text{Co}_3\text{V}_2\text{O}_8@\text{Co-B-2}$ is closest to that of $\text{Co}_3\text{V}_2\text{O}_8$. So does pore volume. A larger surface area and more pores mean more electroactive sites, which is very advantageous to facilitate the diffusion of ions and electrons.

2.3. Electrochemical Performance

Figure 5 compares the electrochemical character of the as-prepared samples. As displayed in Figure 5a, the $\text{Co}_3\text{V}_2\text{O}_8@\text{Co-B-2}$ electrode shows a larger integral area of the CV curve than other electrodes, suggesting that the crystalline-amorphous heterointerface which is produced by the introduction of Co-B can evidently increase the capacitance of the electrode. Figure 5b displayed that the $\text{Co}_3\text{V}_2\text{O}_8@\text{Co-B-2}$ electrode presents a longer discharge time than others. The specific capacitance of the samples as a function of current density is shown in Figure 5c. The specific capacitance of the $\text{Co}_3\text{V}_2\text{O}_8@\text{Co-B-2}$ sample is 552.4 F g^{-1} at 0.5 A g^{-1} and still retains 66.9% initial capacitance at 10 A g^{-1} . The comparison of the specific capacitances and retention rate of $\text{Co}_3\text{V}_2\text{O}_8@\text{Co-B-2}$ with other reported cobalt-based compounds have been added in Table 1. Besides, the electrochemical process kinetics of the electrodes are analyzed according to electrochemical impedance spectroscopy (EIS) and Bode plots.^[48] $\text{Co}_3\text{V}_2\text{O}_8@\text{Co-B-2}$ electrode material exhibits maximum slope and smallest semicircle compared with others, revealing a fast diffusion rate of electrons and great conductivity. Table 2 indicates the fitting data of equivalent circuit elements for $\text{Co}_3\text{V}_2\text{O}_8$, Co-B , and $\text{Co}_3\text{V}_2\text{O}_8@\text{Co-B}$ electrodes. In Figure 5e, at the characteristic

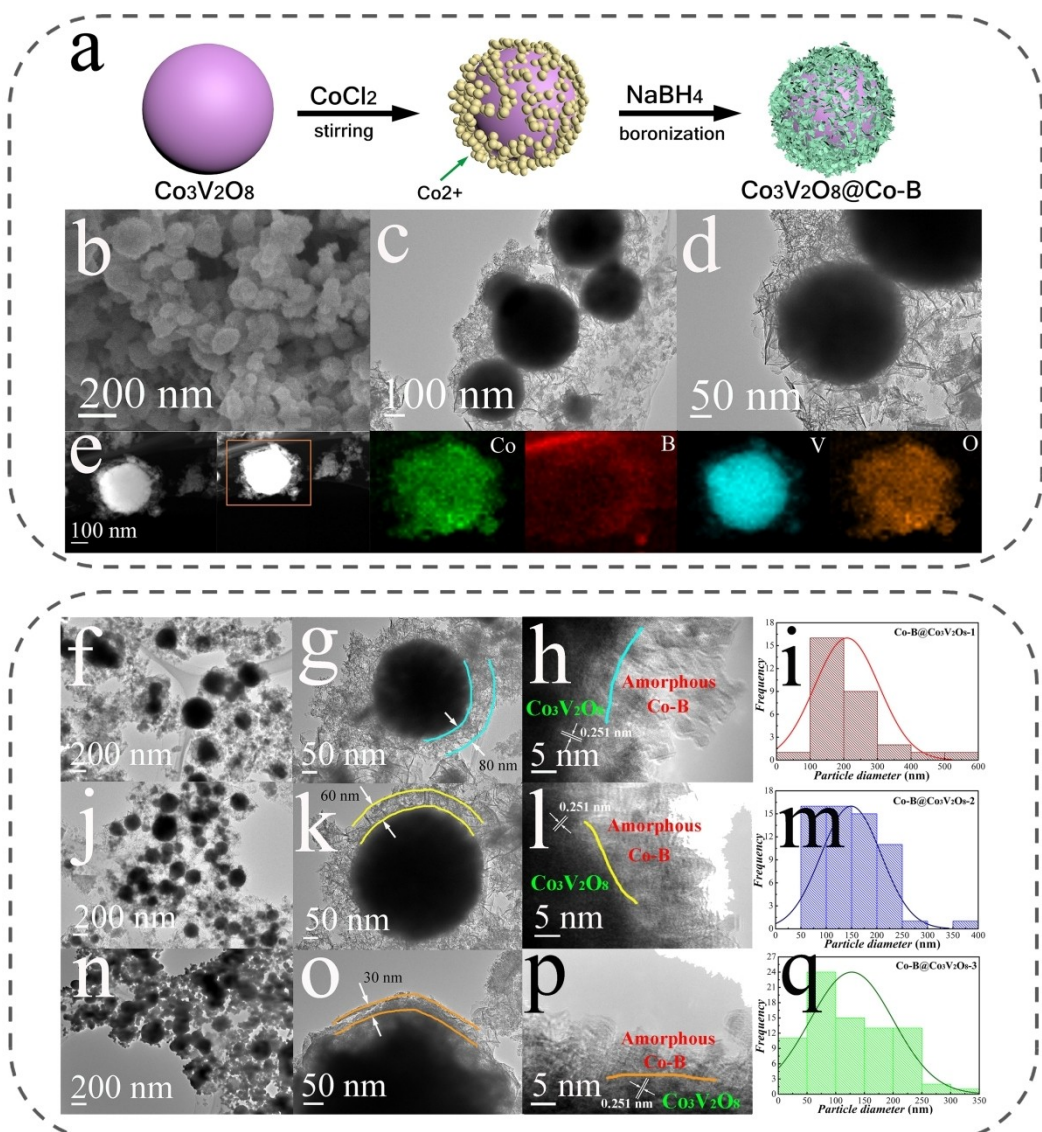


Figure 3. a) Schematic drawing of the formation process; b) SEM, c, d) TEM, and e) Mapping images of the $\text{Co}_3\text{V}_2\text{O}_8@\text{Co-B-2}$ sample; TEM images, particle size distribution and frequency curves of $\text{Co}_3\text{V}_2\text{O}_8@\text{Co-B}$ with different shell thicknesses: f-i) $\text{Co}_3\text{V}_2\text{O}_8@\text{Co-B-1}$, g-m) $\text{Co}_3\text{V}_2\text{O}_8@\text{Co-B-2}$, and n-q) $\text{Co}_3\text{V}_2\text{O}_8@\text{Co-B-3}$.

Table 1. Summarization of the specific capacitances of some electrode materials.

Electrode	Specific capacitance	Retention rate	Ref.
Co-W-B	306.3 Fg^{-1}	52.4% from at 2 Ag^{-1} 1 to 10 Ag^{-1}	[52]
$\text{Co}_3\text{O}_4@\text{CoWO}_4/\text{rGO}$	386 Fg^{-1}	63% from at 0.5 Ag^{-1} 0.5 to 10 Ag^{-1}	[53]
Grapheme/ $\text{Co}_3\text{V}_2\text{O}_8$	528.2 Fg^{-1}	80% from at 0.5 Ag^{-1} 0.5 to 2 Ag^{-1}	[29]
$\text{CoMoO}_4 \cdot 0.9\text{H}_2\text{O}$	377 Fg^{-1}	62.6% from at 0.5 Ag^{-1} 0.5 to 5 Ag^{-1}	[54]
$\text{Co}_3\text{V}_2\text{O}_8@\text{Co-B-2}$	552.4 Fg^{-1}	66.9% from at 0.5 Ag^{-1} 0.5 to 10 Ag^{-1}	This work

frequency corresponding to the -45° phase angle on the vertical axis of the Bode plot, the resistive impedance and the capacitive impedance are equal.^[49] According to the equation

Table 2. Fitting data of equivalent circuit elements of $\text{Co}_3\text{V}_2\text{O}_8$, Co-B, and $\text{Co}_3\text{V}_2\text{O}_8@\text{Co-B}$ electrodes.

Sample	$R_s [\text{m}\Omega]$	$R_{ct} [\text{m}\Omega]$
$\text{Co}_3\text{V}_2\text{O}_8$	441	438
Co-B	354	382
$\text{Co}_3\text{V}_2\text{O}_8@\text{Co-B-1}$	352	386
$\text{Co}_3\text{V}_2\text{O}_8@\text{Co-B-2}$	364	300
$\text{Co}_3\text{V}_2\text{O}_8@\text{Co-B-3}$	383	626

$\tau = 1/f$ to calculate the relaxation time,^[50] it can be seen that among the $\text{Co}_3\text{V}_2\text{O}_8@\text{Co-B}$ samples, the $\text{Co}_3\text{V}_2\text{O}_8@\text{Co-B-2}$ electrode has the largest frequency and the smallest time constant, which indicates that the electrode presents a better electrochemical character. Figure 5f shows the relationship between Co-B content and specific capacitance in the core-shell structure. When the mass ratio of $\text{Co}_3\text{V}_2\text{O}_8$ to Co-B is 2:1, the specific capacitance is the largest. The other curve is based

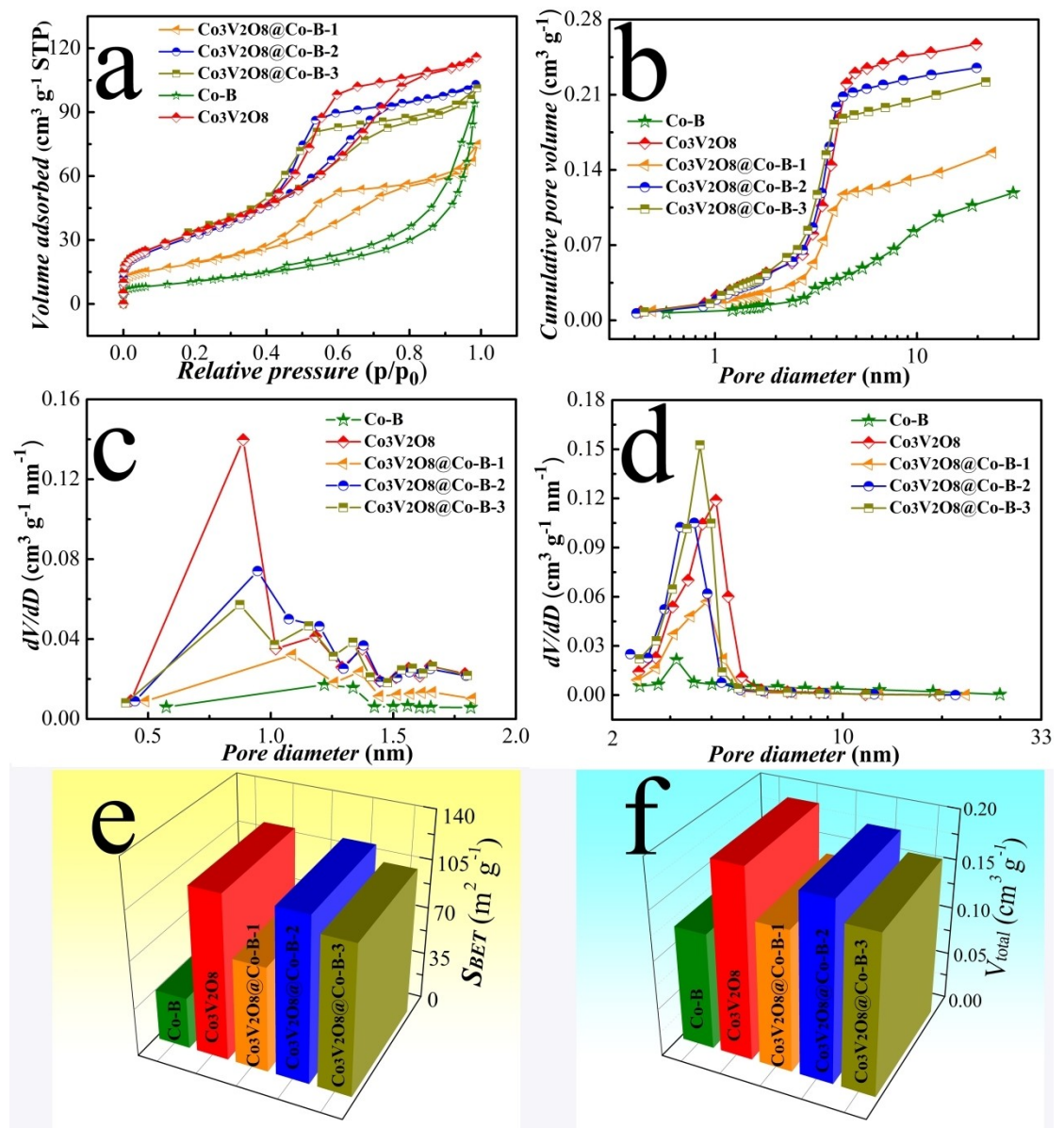


Figure 4. a) N_2 adsorption-desorption isotherm, b) cumulative pore volume, c, d) pore size distribution, e) specific surface areas, and f) pore volume of the samples.

on the equation: $C = 291.1 * a + 321.2 *$ (1a) to calculate the predicted specific capacitance of $\text{Co}_3\text{V}_2\text{O}_8@\text{Co-B}$, where a is the content of Co-B .^[51] Its capacitance is between $\text{Co}_3\text{V}_2\text{O}_8$ and Co-B . It can be seen that there is a big difference between reality and prediction. The increased capacitance comes from the $\text{Co}_3\text{V}_2\text{O}_8@\text{Co-B}$ crystalline-amorphous heterojunction surface, which reduces the diffusion barrier and promotes the transport of carriers and the Faraday reaction process. As shown in Figure 5g, $\text{Co}_3\text{V}_2\text{O}_8$, Co-B , and $\text{Co}_3\text{V}_2\text{O}_8@\text{Co-B-2}$ electrodes exhibit capacitance retention of 82.6%, 71.2%, and 78.3% at 5 A g^{-1} after 10,000 cycles, respectively. Here, the $\text{Co}_3\text{V}_2\text{O}_8@\text{Co-B-2}$ electrode material coated with an amorphous layer did not reach the expected experimental results. The possible reason is that the Faraday redox process of battery-type electrode materials mainly occurs in the bulk phase, while

the charge stored in pseudo-capacitive materials mainly occurs on the surface, and the effect of the amorphous layer in alleviating volume expansion is not prominent. In addition, in the first 4000 cycles, the $\text{Co}_3\text{V}_2\text{O}_8$ electrode material showed an upward trend with an activation process, so the actual cycle performance of $\text{Co}_3\text{V}_2\text{O}_8$ should be lower than 82.6%.

Figure 6a and 6b show the CV profiles of the $\text{Co}_3\text{V}_2\text{O}_8$ and Co-B electrodes at 5 mVs^{-1} , respectively. Two pairs of anodic and cathodic peaks are clearly observed in the CV profiles, indicating the pseudocapacitance features of both electrodes. In Figure 6c, We summed the CV curves of $\text{Co}_3\text{V}_2\text{O}_8$ and Co-B to obtain the summed CV curve of the $\text{Co}_3\text{V}_2\text{O}_8@\text{Co-B}$ electrode.^[55] The summed CV curve (blue dotted lines) represented an idealized state, in which $\text{Co}_3\text{V}_2\text{O}_8$ and Co-B fully contributed their capacitance. The summed curve is compared

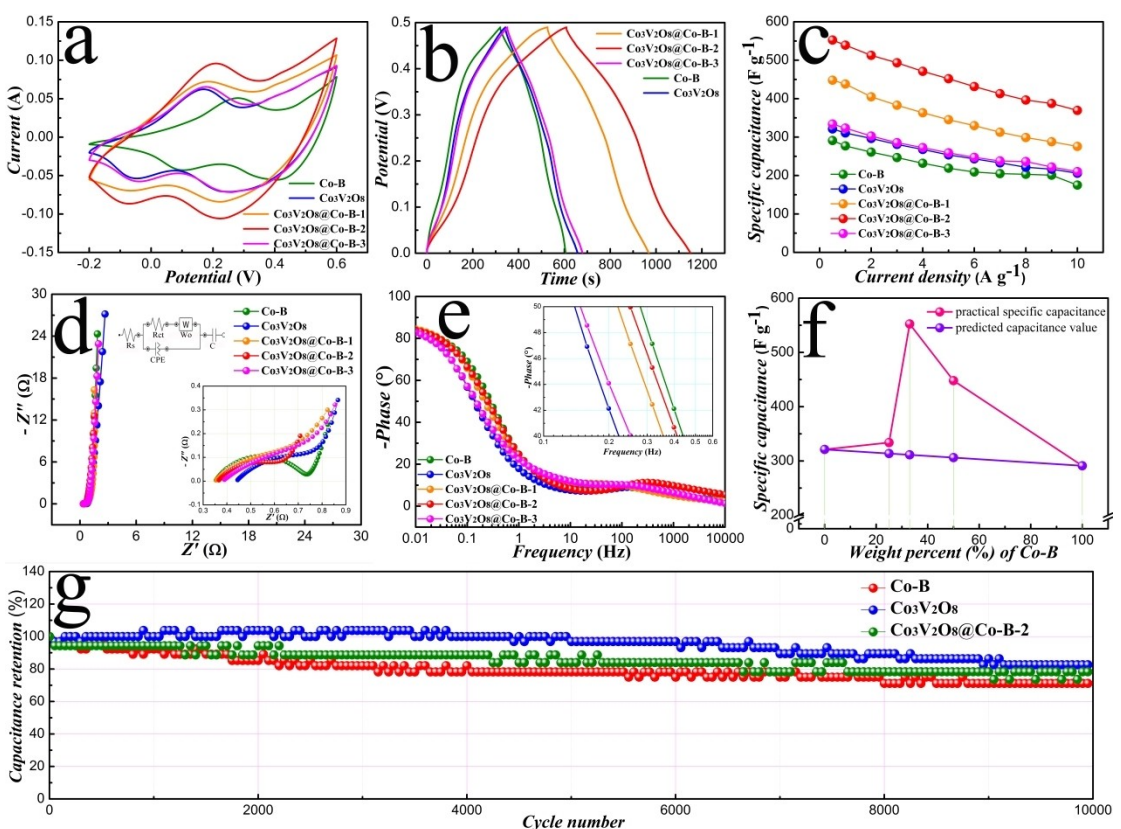
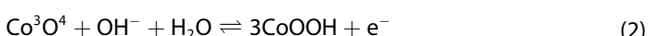
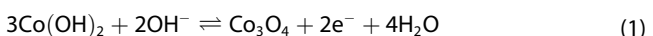


Figure 5. Electrochemical characterizations of as-prepared electrodes: a) CV curves at 50 mV s^{-1} , b) GCD curves at 0.5 A g^{-1} , c) specific capacitance, d) Nyquist plots, e) impedance Bode plots, f) relationship between Co–B content and specific capacitance in core–shell structure, and g) cycling performance.

with the actual curve (Figure 6d), and the results exhibit that the shape of the actual CV curve is close to the summed CV curve. The actual CV curve represented $\text{Co}_3\text{V}_2\text{O}_8$ and Co–B both participate in the electrode redox reaction and contribute to their capacitance. So far, there has been a lot of investigation on cobalt-based electrodes for supercapacitors. Here, according to relevant works of literature, a possible reaction mechanism is proposed and described [Eqs. (1) and (2)].^[56]



In the alkaline solution, Co–B, $\text{Co}_3\text{V}_2\text{O}_8$, and $\text{Co}_3\text{V}_2\text{O}_8@\text{Co–B}$ first convert to $\text{Co}(\text{OH})_2$ under a relatively high potential. The pair of redox reaction peaks with the anodic peak at Peak I and the cathodic peak at Peak IV can be attributed to the redox reaction (eq 1). The anodic peak at Peak II corresponds to the cathodic peak at Peak III, attributing to the nearby electrode potential of the redox reactions (eq 2).

The excellent electrochemical properties of the $\text{Co}_3\text{V}_2\text{O}_8@\text{Co–B}$ electrode can be attributed to the morphology and crystal structural benefits of the composite, which provides multiple advantages for high performance. The morphology and crystal structure evolution of $\text{Co}_3\text{V}_2\text{O}_8$, Co–B, and $\text{Co}_3\text{V}_2\text{O}_8@\text{Co–B}$ electrodes are shown in Figure 7. In Figure 7a, the shell layer of $\text{Co}_3\text{V}_2\text{O}_8@\text{Co–B}$ is interconnected Co–B

nanoflakes, which not only improves the electronic conductivity of the hybrid but promotes the reversibility of the conversion reaction. Space to suppress volume fluctuations can greatly increase the diffusion rate of the electrolyte. This brings high capacity and stable cycle performance. The $\text{Co}_3\text{V}_2\text{O}_8$ nanospheres in the core layer have a porous structure, which allows the electrolyte to fully penetrate and has more charge storage sites, which facilitates ion transport and produces excellent rate capacity. However, $\text{Co}_3\text{V}_2\text{O}_8$ nanoparticles are difficult to achieve high capacity due to low conductivity, and the unstable structure of Co–B nanoflakes leads to low cycle stability. In addition, the core layer $\text{Co}_3\text{V}_2\text{O}_8$ has a stable crystal structure, which can make full use of the amorphous structure of the shell layer Co–B to reduce the risk of fracture during the cycle and provide the structural buffer space. The crystal–amorphous contact interface of the $\text{Co}_3\text{V}_2\text{O}_8@\text{Co–B}$ core–shell structure can also reduce the tunneling barrier and facilitate electron transfer and ion diffusion.

The CV curves of the $\text{Co}_3\text{V}_2\text{O}_8@\text{Co–B–2}$ electrode in the voltage window of -0.2 – 0.6 V are shown in Figure 8a.^[57] Two pairs of redox peaks are visible in each scan. The CV profiles disclose the pseudocapacitance characteristics of the $\text{Co}_3\text{V}_2\text{O}_8@\text{Co–B–2}$. The GCD curves of the $\text{Co}_3\text{V}_2\text{O}_8@\text{Co–B–2}$ electrode are measured in a potential window of 0 – 0.49 V. As displayed in Figure 8b, these GCD curves all display an approximately triangular in shape, suggesting the Pseudocapacitance behavior of the sample, which is consistent with its CV

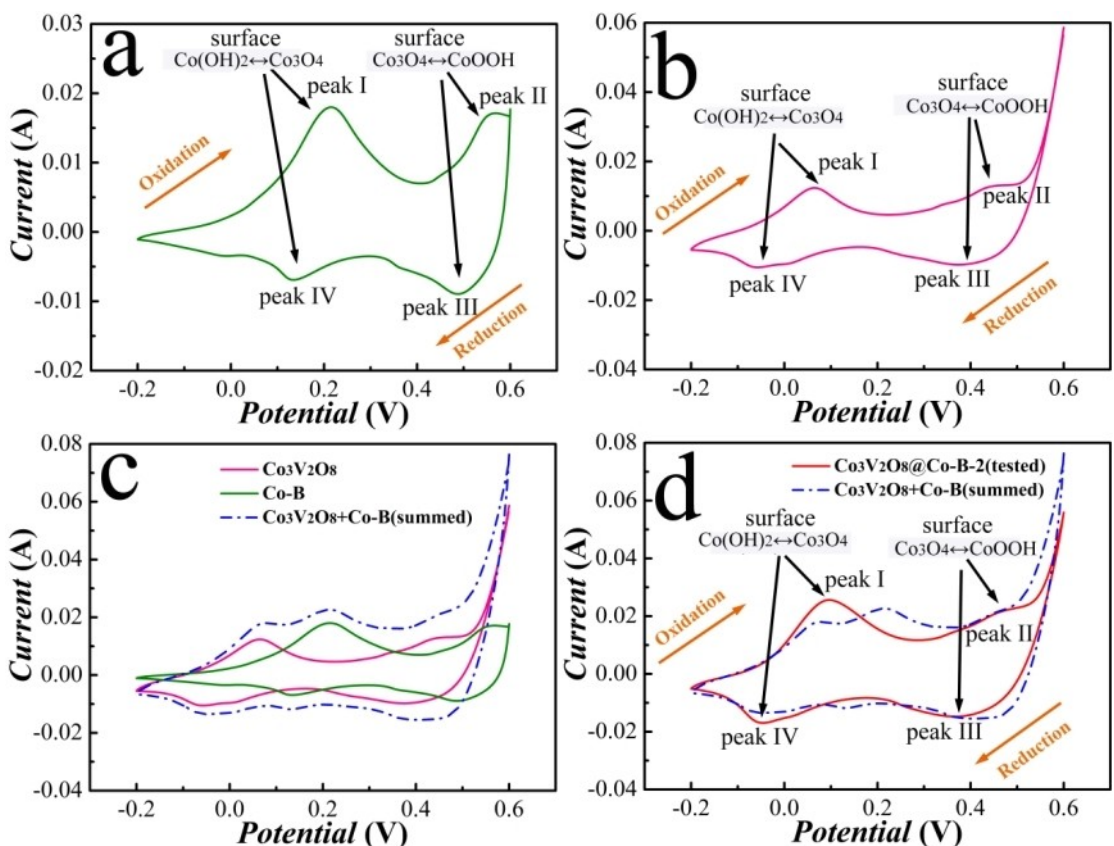


Figure 6. The redox peaks of CV curves at 5 mV s^{-1} : a) $\text{Co}_3\text{V}_2\text{O}_8$ and b) Co–B; c) the summed CV curve by summing CV curves of $\text{Co}_3\text{V}_2\text{O}_8$ and Co–B electrode, d) comparison of the summed CV curve with the real CV curve of $\text{Co}_3\text{V}_2\text{O}_8@\text{Co-B-2}$ electrode.

curves. By plotting the logarithm of the peak current versus the logarithm of the scan rate (Figure 8c), within the scan rate range of $5\text{--}100 \text{ mV s}^{-1}$, the b values of the four peaks are calculated as 0.62, 0.76, 0.74, 0.76, respectively. Figure 7d shows the relationship between the peak current and the square root of the sweep speed, showing a good linear increasing relationship, which is also a typical feature of porous electrodes. This indicates that the entire charge storage process of the electrode is controlled through surface capacitance and diffusion.^[58–59] Figure 8e illustrates the distribution of the ion diffusion and capacitance process of $\text{Co}_3\text{V}_2\text{O}_8@\text{Co-B-2}$ at 20 mV s^{-1} . Obviously, an increased scan rate will increase the proportion of capacitive contribution, while the proportion of diffusion contribution will decrease (Figure 8f). The superior performance of $\text{Co}_3\text{V}_2\text{O}_8@\text{Co-B-2}$ is attributed to the electronic tuning of the redox treatment, which can simultaneously improve the ion diffusion ability and capacitance.

2.4. Electrochemical Performance of the Hybrid Supercapacitors

We manifest the superiority of our $\text{Co}_3\text{V}_2\text{O}_8@\text{Co-B-2}$ sample for high-performance device by assembling an asymmetric supercapacitor (ASC) device with activated carbon (AC) $\text{Co}_3\text{V}_2\text{O}_8@\text{Co-B-2}$ electrode, in which $\text{Co}_3\text{V}_2\text{O}_8@\text{Co-B-2}$ as the

positive electrode and AC as the negative electrode, respectively (Figure 9a). Figure S3 is the CV curves of $\text{Co}_3\text{V}_2\text{O}_8@\text{Co-B-2}$ electrode with a potential window of -0.2 to 0.6 V and AC electrode with -1 to 0 V . Thereby, it is possible that the voltage range of this ASC extends up to 1.6 V in 6 M KOH electrolyte. As exhibited in Figure 9b and 8c, the CV and GCD curves of different potential window are collected at 10 mV s^{-1} and 0.25 A g^{-1} , respectively, proving that ASC has pseudocapacitance even in the 1.6 V potential range. In Figure 9d, all the profiles at various scan rates have similar shapes and the inside area becomes larger with higher scan rates. This result is satisfactory to indicate that the $\text{Co}_3\text{V}_2\text{O}_8@\text{Co-B-2//AC}$ ASC has a superior fast charge-discharge character. According to the GCD curve in Figure 9e, the specific capacitances of the assembled device under various current densities are calculated. The specific capacitance is calculated to be 75.91 F g^{-1} at 0.25 A g^{-1} . EIS of the device is displayed in Figure 9g, it is obviously found that $\text{Co}_3\text{V}_2\text{O}_8@\text{Co-B-2//AC}$ device shows a low impedance R_{ct} of 1.3Ω , which can promote the electron transfer. Figure 9h presents that the rate capability of the device is 96.55% after 10,000 cycles. The Ragone plot (Figure 9i) of $\text{Co}_3\text{V}_2\text{O}_8@\text{Co-B-2//AC}$ ASC is derived from GCD, which reveals the relationship between energy density and power density. The ASC device exhibits a high energy density of 27 Wh kg^{-1} at 200 W kg^{-1} and a great power density of 8000 W kg^{-1} at 18 Wh kg^{-1} . Our device shows pretty good

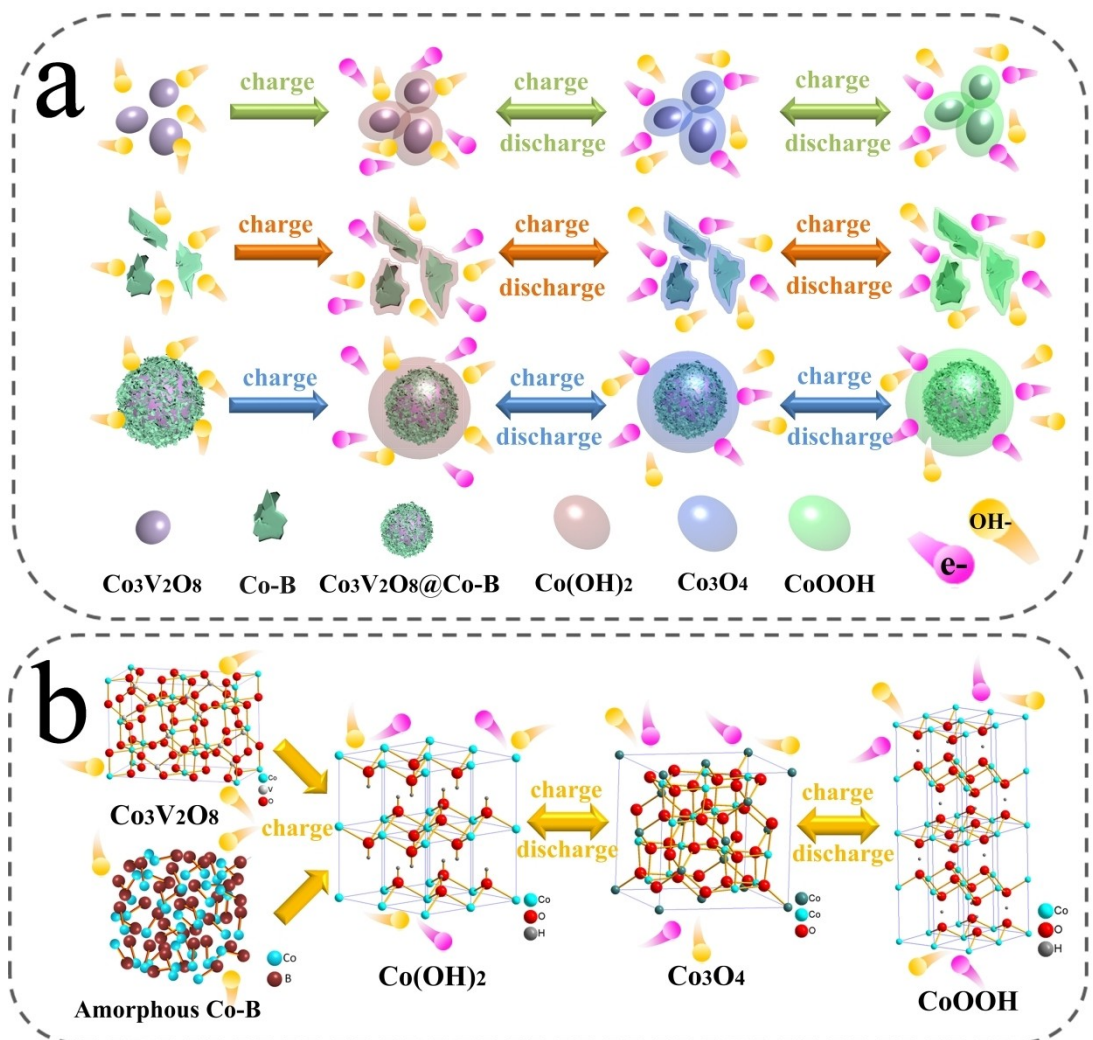


Figure 7. a) Schematic drawing of the morphology and b) crystal structure evolutions of $\text{Co}_3\text{V}_2\text{O}_8$ nanoparticles, Co-B nanoflakes, and $\text{Co}_3\text{V}_2\text{O}_8@\text{Co-B}$ electrodes.

performance compared with the other ASC devices reported in recent years.^[14,53,60–61] In addition, we will further expand the application of the ASC device in real-life in the next work.^[62–63]

3. Conclusions

In general, we have rationally designed a crystalline $\text{Co}_3\text{V}_2\text{O}_8@\text{amorphous Co-B}$ core-shell nanostructure with a tunable shell thickness via water bath and liquid phase reduction process. The $\text{Co}_3\text{V}_2\text{O}_8@\text{Co-B-2}$ displayed excellent electrochemical properties with high specific capacitance, long cycling life, as well as great rate capability. The method provides a simple, economical, and convenient method to obtain crystal-amorphous heterogeneous nanostructures that can realize the rapid transfer of ions and electrons in practical applications for energy storage and conversion devices, such as the lithium-ion battery, electrocatalysis, etc.

Experimental Section

Materials

All reagents in this study were analytic grade, and all solutions used throughout the experiments were ultrapure water. Sinopharm Chemical Reagent Co., Ltd. (Shanghai, China) had provided Cobalt Chloride Hexahydrate ($\text{CoCl}_2 \cdot 6\text{H}_2\text{O}$, > 99%), Sodium Orthovanadate dodecahydrate ($\text{Na}_3\text{O}_4\text{V} \cdot 12\text{H}_2\text{O}$, > 99%), Sodium Borohydride (NaBH_4 , > 99%), Sodium Hydroxide (NaOH) and Anhydrous Ethanol ($\text{C}_2\text{H}_5\text{OH}$).

Preparation of $\text{Co}_3\text{V}_2\text{O}_8$ nanoparticles

3 mmol $\text{CoCl}_2 \cdot 6\text{H}_2\text{O}$ was dispersed in 80 mL ultrapure water at 70 °C under uniform stirring. 2 mmol $\text{Na}_3\text{O}_4\text{V} \cdot 12\text{H}_2\text{O}$ was dissolved into the above solution subsequently and stirred continually for 6 h. The resulting brown precipitates were cleaned with ultrapure water and ethanol several times and collected by centrifugation as well as dried in vacuum at 60 °C for 12 h.

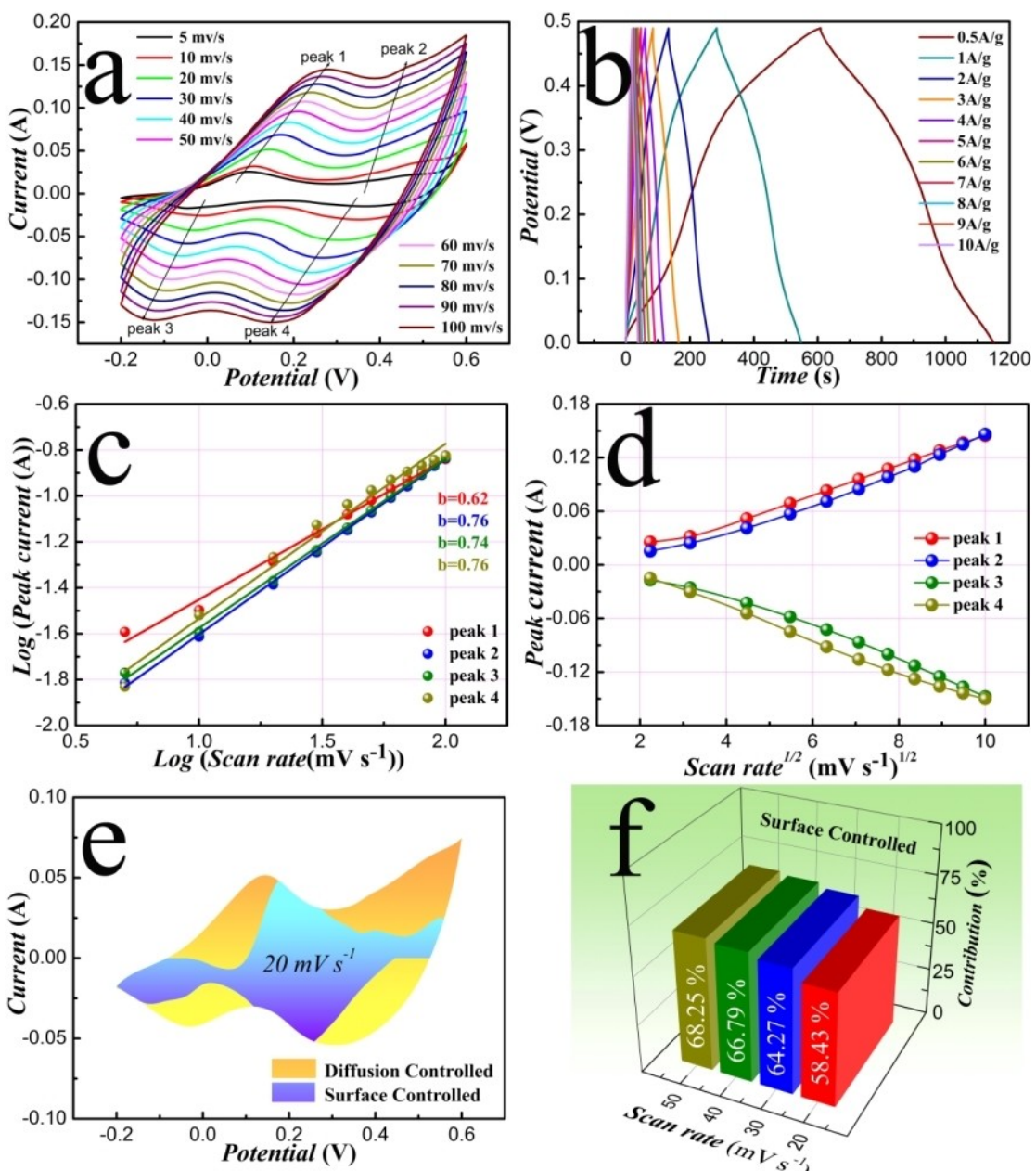


Figure 8. Electrochemical kinetic analysis of $\text{Co}_3\text{V}_2\text{O}_8@\text{Co-B-2}$ Electrode: a) CV curves, b) GCD curves, c) b-values determination of cathodic and anodic peaks, d) the relationship curve between peak current and square root of sweep speed, e) separation of the capacitive and diffusion-controlled current contribution at 20 mVs^{-1} , f) contribution ratio of capacitive and diffusion controlled capacitances.

Preparation of Co-B

The Co-B nanoflake was synthesized by reducing $\text{CoCl}_2 \cdot 6\text{H}_2\text{O}$ in action of a strong reducing agent NaBH_4 . The detailed experimental procedure is as follows: 40 ml of an aqueous solution of 4 mmol $\text{CoCl}_2 \cdot 6\text{H}_2\text{O}$ in a round-bottomed Schlenk flask was deaerated, flushed with N_2 to remove the dissolved oxygen. An ice bath was used to control the reaction temperature. 10 mmol NaBH_4 dispersed in 20 mL 0.1 M NaOH solution deaerated with N_2 , and then slowly added to CoCl_2 with a syringe. Aqueous solution black instantaneously with lots of effervescence. Once the bubble generation ceases, the black precipitate was collected by filtration which was extensively washed with ultrapure water and ethanol

and dried by vacuum-drying technology. The weight of the synthesized Co-B is 0.28 g.

Preparation of crystalline $\text{Co}_3\text{V}_2\text{O}_8@\text{amorphous cobalt boride heterostructures with different core@shell size ratio}$

$\text{Co}_3\text{V}_2\text{O}_8@\text{Co-B}$ was prepared by a facile liquid phase reduction reaction. 0.14, 0.28, 0.42 g of $\text{Co}_3\text{V}_2\text{O}_8$ nanoparticles dispersed in 40 mL 0.05 M $\text{CoCl}_2 \cdot 6\text{H}_2\text{O}$ solution deaerated with N_2 , respectively. Subsequently, 10 mL of 0.5 M NaBH_4 aqueous solution which had been removed the dissolved oxygen by purging N_2 was added into the above solution with a syringe. After stirring for 1 h, the mixture solution was collected by filtration and rinsed alternately with water and ethanol. And then the $\text{Co}_3\text{V}_2\text{O}_8@\text{Co-B}$ was obtained by

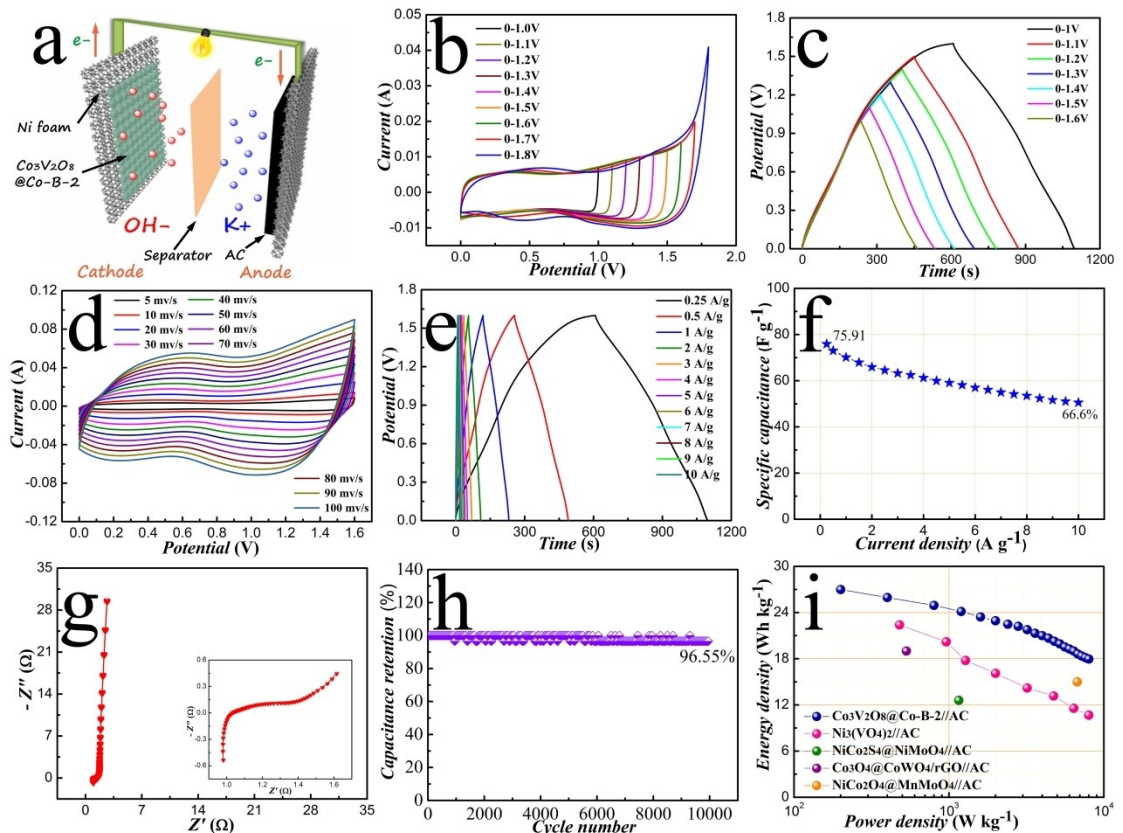


Figure 9. a) Electrochemical characterizations of ASC. Schematic illustration, b, c) CV and GCD profiles over various voltage windows at 10 mV s^{-1} and 0.25 A g^{-1} , respectively, d) CV curves, e) GCD curves, and f) specific capacitance, g) Nyquist plots, h) cycling stability, i) Ragone plots.

vacuum-drying technology. The mass of $\text{Co}_3\text{V}_2\text{O}_8$ was used to control the core@shell size ratio. The composite materials with a mass ratio of $\text{Co}_3\text{V}_2\text{O}_8$ and Co–B of 1:1, 2:1, and 3:1 were named $\text{Co}_3\text{V}_2\text{O}_8 @ \text{Co-B-1}$, $\text{Co}_3\text{V}_2\text{O}_8 @ \text{Co-B-2}$, and $\text{Co}_3\text{V}_2\text{O}_8 @ \text{Co-B-3}$, respectively.

Supporting Information

Additional references cited with the Supporting Information.^[64–68]

Acknowledgments

This work was supported by the National Natural Science Foundation of China (No. 51971104, 51762031).

Conflict of Interest

The authors declare no conflict of interest.

Keywords: core-shell nanostructured · crystalline/amorphous interface · cobalt vanadium oxide · energy storage

- [1] J. C. Zhang, B. Q. Yuan, S. F. Cui, N. N. Zhang, J. J. Wei, X. Wang, D. J. Zhang, R. C. Zhang, Q. S. Huo, *Dalton Trans.* **2017**, *46*, 3295–3302.
- [2] Y. Cheng, Y. Zhang, H. Jiang, X. Dong, C. Meng, Z. Kou, *J. Power Sources* **2020**, *448*, 227407.
- [3] C. Li, Q. Zhang, J. Sun, T. Li, S. E. Z. Zhu, B. He, Z. Zhou, Q. Li, Y. Yao, *ACS Energy Lett.* **2018**, *3*, 2761–2768.
- [4] Y. F. Teng, Y. D. Li, D. Y. Yu, Y. N. Meng, Y. P. Wu, X. D. Zhao, X. Y. Liu, *ChemistrySelect* **2019**, *4*, 956–962.
- [5] S. Zhao, K. Tao, Y. Gong, *Dalton Trans.* **2019**, *48*, 5315–5326.
- [6] Y. Li, M. Chen, B. Liu, Y. Zhang, X. Liang, X. Xia, *Adv. Energy Mater.* **2020**, *10*, 2000927.
- [7] R. Liu, A. Zhou, X. Zhang, J. Mu, H. Che, Y. Wang, T.-T. Wang, Z. Zhang, Z. Kou, *Chem. Eng. J.* **2021**, *412*, 128611.
- [8] K. Chi, Z. Y. Zhang, Q. Y. Lv, C. Y. Xie, J. Xiao, F. Xiao, S. Wang, *ACS Appl. Mater. Interfaces* **2017**, *9*, 6044–6053.
- [9] V. T. V. Chebrolu, B. Balakrishnan, I. Cho, J. S. Bak, H. J. Kim, *Dalton Trans.* **2019**, *48*, 8254–8263.
- [10] G. J. He, J. M. Li, W. Y. Li, B. Li, N. Noor, K. B. Xu, J. Q. Hu, I. P. Parkin, *J. Mater. Chem. A* **2015**, *3*, 14272–14278.
- [11] Y. Chen, T. Zhou, L. Li, W. K. Pang, X. He, Y.-N. Liu, Z. Guo, *ACS Nano* **2019**, *13*, 9376–9385.
- [12] C. L. Xiang, Q. Y. Wang, Y. J. Zou, P. R. Huang, H. L. Chu, S. J. Qiu, F. Xu, L. X. Sun, *J. Mater. Chem. A* **2017**, *5*, 9907–9916.
- [13] Q. Zhang, W. Xu, J. Sun, Z. Pan, J. Zhao, X. Wang, J. Zhang, P. Man, J. Guo, Z. Zhou, B. He, Z. Zhang, Q. Li, Y. Zhang, L. Xu, Y. Yao, *Nano Lett.* **2017**, *17*, 7552–7560.
- [14] R. Kumar, P. Rai, A. Sharma, *J. Mater. Chem. A* **2016**, *4*, 9822–9831.
- [15] S. Kumar, G. Saeed, N. H. Kim, J. H. Lee, *J. Mater. Chem. A* **2018**, *6*, 7182–7193.
- [16] Z. Zhou, Q. Zhang, J. Sun, B. He, J. Guo, Q. Li, C. Li, L. Xie, Y. Yao, *ACS Nano* **2018**, *12*, 9333–9341.
- [17] C. Q. Teng, X. H. Gao, N. Zhang, Y. Jia, X. Y. Li, Z. Y. Shi, Z. X. Wu, M. J. Zhi, Z. L. Hong, *RSC Adv.* **2018**, *8*, 32979–32984.
- [18] N. X. Shi, S. L. Xiong, F. F. Wu, J. Bai, Y. T. Chu, H. Z. Mao, J. K. Feng, B. J. Xi, *Eur. J. Inorg. Chem.* **2017**, 734–740.

- [19] L. Q. Mai, F. Yang, Y. L. Zhao, X. Xu, L. Xu, Y. Z. Luo, *Nat. Commun.* **2011**, 2.
- [20] Z. R. Lou, Y. G. Li, L. P. Zhu, W. Y. Xie, W. Z. Niu, H. Song, Z. Z. Ye, S. B. Zhang, *J. Mater. Chem. A* **2017**, 5, 2732–2738.
- [21] S. T. Fu, J. Chen, X. X. Wang, Q. He, S. F. Tong, M. M. Wu, *Small* **2020**, 16.
- [22] S. Sun, T. Zhai, C. Liang, S. V. Savilov, H. Xia, *Nano Energy* **2018**, 45, 390–397.
- [23] J. J. Deng, X. L. Yu, X. Y. Qin, D. Zhou, L. H. Zhang, H. Duan, F. Y. Kang, B. H. Li, G. X. Wang, *Adv. Energy Mater.* **2019**, 9.
- [24] Q. Y. Wang, Y. M. Luo, R. Z. Hou, S. Zaman, K. Qi, H. F. Liu, H. S. Park, B. Y. Xia, *Adv. Mater.* **2019**, 31, 1905744.
- [25] C. Lu, P. R. Jothi, T. Thersleff, T. M. Budnyak, A. Rokicinska, K. Yubuta, R. Dronkowski, P. Kuśtrowski, B. P. T. Fokwa, A. Slabon, *Nanoscale* **2020**, 12, 3121–3128.
- [26] G. Nie, Y. Luan, Z. Kou, J. Jiang, Z. Zhang, N. Yang, J. Wang, Y.-Z. Long, *J. Colloid Interface Sci.* **2021**, 582, 543–551.
- [27] I. Hussain, A. Ali, C. Lamiel, S. G. Mohamed, S. Sahoo, J. J. Shim, *Dalton Trans.* **2019**, 48, 3853–3861.
- [28] S. Gupta, N. Patel, A. Miotello, D. C. Kothari, *J. Power Sources* **2015**, 279, 620–625.
- [29] W. H. Low, C. W. Siong, C. H. Chia, S. S. Lim, P. S. Khiew, *J. Sci-Adv Mater Dev* **2019**, 4, 515–523.
- [30] J. Yang, M. Wu, F. Gong, T. Feng, C. Chen, J. Liao, *RSC Adv.* **2017**, 7, 24418–24424.
- [31] Y. Y. Jiang, Y. T. Fang, C. X. Chen, P. J. Ni, B. Kong, Z. Q. Song, Y. Z. Lu, L. Niu, *ChemElectroChem* **2019**, 6, 3684–3689.
- [32] J. M. V. Nsanizima, Y. Peng, Y. Y. Xu, L. Thia, C. Wang, B. Y. Xia, X. Wang, *Adv. Energy Mater.* **2018**, 8.
- [33] W. Lu, T. Liu, L. Xie, C. Tang, D. Liu, S. Hao, F. Qu, G. Du, Y. Ma, A. M. Asiri, X. Sun, *Small* **2017**, 13.
- [34] Z. Kou, B. Guo, Y. Zhao, S. Huang, T. Meng, J. Zhang, W. Li, I. S. Amiinu, Z. Pu, M. Wang, M. Jiang, X. Liu, Y. Tang, S. Mu, *ACS Appl. Mater. Interfaces* **2017**, 9, 3702–3712.
- [35] Z. Kou, T. Meng, B. Guo, I. S. Amiinu, W. Li, J. Zhang, S. Mu, *Adv. Funct. Mater.* **2017**, 27, 1604904.
- [36] A. M. Zardkhoshouei, S. S. H. Davarani, M. Hashemi, *New J. Chem.* **2019**, 43, 4590–4598.
- [37] J. S. Li, C. X. Zhao, Y. X. Yang, C. F. Li, T. Hollenkamp, N. Burke, Z. Y. Hu, G. Van Tendeloo, W. Chen, *J. Alloys Compd.* **2019**, 810.
- [38] X. Gao, X. Liu, D. Wu, B. Qian, Z. Kou, Z. Pan, Y. Pang, L. Miao, J. Wang, *Adv. Funct. Mater.* **2019**, 29, 1903879.
- [39] M. Wu, J. Yang, T. Feng, W. Jiang, D. Xia, F. Gong, J. Liao, *New J. Chem.* **2017**, 41, 10634–10639.
- [40] V. Soundharrajan, B. Sambandam, J. Song, S. Kim, J. Jo, S. Kim, S. Lee, V. Mathew, J. Kim, *ACS Appl. Mater. Interfaces* **2016**, 8, 8546–8553.
- [41] B. B. Hu, Y. Cen, C. L. Xu, Q. Xiang, M. K. Aslam, L. J. Liu, S. Li, Y. P. Liu, D. M. Yu, C. G. Chen, *Nanoscale* **2020**, 12, 3763–3776.
- [42] W. B. Lu, T. T. Liu, L. S. Xie, C. Tang, D. N. Liu, S. Hao, F. L. Qu, G. Du, Y. J. Ma, A. M. Asiri, X. P. Sun, *Small* **2017**, 13.
- [43] S. Gupta, N. Patel, R. Fernandes, R. Kadrekar, A. Dashora, A. K. Yadav, D. Bhattacharyya, S. N. Jha, A. Miotello, D. C. Kothari, *Appl Catal B-Environ* **2016**, 192, 126–133.
- [44] Q. Zhang, J. Zhao, Y. Wu, J. Li, H. Jin, S. Zhao, L. Chai, Y. Wang, Y. Lei, S. Wang, *Small* **2020**.
- [45] J. J. Yan, H. Wang, S. Ji, B. G. Pollet, R. F. Wang, *Nanoscale* **2018**, 10, 7813–7820.
- [46] J. Deng, X. Yu, X. Qin, D. Zhou, L. Zhang, H. Duan, F. Kang, B. Li, G. Wang, *Adv. Energy Mater.* **2019**, 9, 1803612.
- [47] N. Hu, W. H. Gong, L. Huang, P. K. Shen, *J. Mater. Chem. A* **2019**, 7, 1273–1280.
- [48] B. He, P. Man, Q. Zhang, H. Fu, Z. Zhou, C. Li, Q. Li, L. Wei, Y. Yao, *Nano-Micro Lett.* **2019**, 11, 101.
- [49] F. L. Qi, Z. X. Xia, R. L. Sun, X. J. Sun, X. L. Xu, W. Wei, S. L. Wang, G. Q. Sun, *J. Mater. Chem. A* **2018**, 6, 14170–14177.
- [50] G. Nie, X. Zhao, J. Jiang, Y. Luan, J. Shi, J. Liu, Z. Kou, J. Wang, Y.-Z. Long, *Chem. Eng. J.* **2020**, 402, 126294.
- [51] Q. E. Zhang, A. A. Zhou, J. Wang, J. Wu, H. Bai, *Energy Environ. Sci.* **2017**, 10, 2372–2382.
- [52] Y. Yin, C. L. Xiang, H. L. Chu, H. Z. Zhang, F. Xu, E. H. Yan, L. X. Sun, C. Y. Tang, Y. J. Zou, *Appl. Surf. Sci.* **2018**, 460, 25–32.
- [53] X. W. Xu, Y. Yang, M. Wang, P. Dong, R. Baines, J. F. Shen, M. X. Ye, *Ceram. Int.* **2016**, 42, 10719–10725.
- [54] L. R. Hou, H. Hua, S. J. Liu, G. Pang, C. Z. Yuan, *New J. Chem.* **2015**, 39, 5507–5512.
- [55] Q. Y. Dou, L. Y. Liu, B. J. Yang, J. W. Lang, X. B. Yan, *Nat. Commun.* **2017**, 8.
- [56] X. J. Chen, M. Cheng, D. Chen, R. M. Wang, *ACS Appl. Mater. Interfaces* **2016**, 8, 3892–3900.
- [57] X. J. Ma, L. B. Kong, W. B. Zhang, M. C. Liu, Y. C. Luo, L. Kang, *Electrochim. Acta* **2014**, 130, 660–669.
- [58] M. Chen, H. Fan, Y. Zhang, X. Liang, Q. Chen, X. Xia, *Small* **2020**, 16, 2003434.
- [59] Y. M. Hu, M. C. Liu, Y. X. Hu, Q. Q. Yang, L. B. Kong, L. Kang, *Electrochim. Acta* **2016**, 215, 114–125.
- [60] Y. L. Yuan, W. C. Wang, J. Yang, H. C. Tang, Z. Z. Ye, Y. J. Zeng, J. G. Lu, *Langmuir* **2017**, 33, 10446–10454.
- [61] Y. Zhang, J. Xu, Y. Y. Zheng, Y. J. Zhang, X. Hu, T. T. Xu, *Nanoscale Res. Lett.* **2017**, 12.
- [62] L. Zhang, Y. Li, S. Zhang, X. Wang, X. Xia, D. Xie, C. Gu, J. Tu, *Small Methods* **2019**, 3, 1900383.
- [63] J. Zhang, Y. Li, M. Han, Q. Xia, Q. Chen, M. Chen, *Mater. Res. Bull.* **2021**, 137, 111186.
- [64] J. F. Gao, W. B. Zhang, Z. Y. Zhao, L. B. Kong, *Sustain. Energy Fuels* **2018**, 2, 1178–1188.
- [65] M. C. Liu, L. B. Kong, L. Kang, X. H. Li, F. C. Walsh, M. Xing, C. Lu, X. J. Ma, Y. C. Luo, *J. Mater. Chem. A* **2014**, 2, 4919–4926.
- [66] K. Tao, Y. J. Yang, C. Yang, Q. X. Ma, L. Han, *Dalton Trans.* **2019**, 48, 14156–14163.
- [67] H. Wang, J. J. Yan, R. F. Wang, S. X. Li, D. J. L. Brett, J. L. Key, S. Ji, *J. Mater. Chem. A* **2017**, 5, 92–96.
- [68] Z. Zhang, Y. D. Liu, Z. Y. Huang, L. Ren, X. Qi, X. L. Wei, J. X. Zhong, *Phys. Chem. Chem. Phys.* **2015**, 17, 20795–20804.

Manuscript received: January 23, 2021

Revised manuscript received: February 11, 2021

Accepted manuscript online: February 19, 2021

Version of record online: March 3, 2021